Light-Induced Electron Spin Polarization of a Weakly Coupled Triplet−Doublet Spin Pair in a Covalently Linked Porphyrin Dimer

Art van der Est,*,† Motoko Asano-Someda,*,‡ Paul Ragogna,† and Youkoh Kaizu‡

Department of Chemistry, Brock University, 500 Glenridge Avenue, St. Catharines, Ontario, Canada L2S 3A1, and Department of Chemistry, Tokyo Institute of Technology, O-okayama, Meguro-ku, Tokyo, 152-8551, Japan

Received: January 25, 2002; In Final Form: June 25, 2002

The spin-polarization patterns of a weakly coupled triplet−doublet spin pair are studied in a covalently linked copper (II)−free base porphyrin dimer partially oriented in a liquid crystalline solvent. The triplet−doublet pair is generated in the dimer by either spin−orbit intersystem crossing (ISC) within the free-base moiety or via energy transfer (EnT) from the copper porphyrin. The two pathways result in two different spin-polarization patterns, which can be observed separately by selectively exciting either the free base porphyrin at 640 nm or the copper porphyrin at 540 nm. The time development and orientation dependence of the two spin-polarization patterns is investigated at two microwave frequencies. An analysis of the EPR transients reveals that the polarization associated with the EnT pathway rises monoexponentially, while the ISC polarization rises rapidly and decays biexponentially. The rise of the EnT polarization pattern and the fast decay component of the polarization from ISC are governed by the same characteristic lifetime of 2 μs independent of the molecular orientation. However, the ratio of the two decay components of the ISC polarization is strongly orientation dependent. Separately, a general treatment of the spin-polarized transient EPR spectra of coupled triplet−doublet spin pairs is presented and two possible mechanisms for the kinetic behavior involving spin-selective depopulation or relaxation between the spin sublevels of the triplet−doublet pair are investigated. It is shown that all the observed features of the polarization patterns including orientation and excitation wavelength dependence as well as the kinetics can be explained in terms of the model and are consistent with either of the two mechanisms. In addition to the weakly coupled triplet−doublet pair, narrow signal components are observed near the center of the spectrum. The microwave frequency dependence of the spectra confirms the previous assignment that these components are the quartet and doublet states of a strongly coupled triplet−doublet pair generated in conformations of the dimer in which the two porphyrins are in close proximity.

1. Introduction

Electron spin polarization is an integral part of most light induced processes and it has been studied extensively using time-resolved electron paramagnetic resonance spectroscopy (EPR).[1,2] In liquid solution, the radical products of photolysis reactions are usually observed and the spin polarization, which is often referred to as "chemically induced dynamic electron polarization" (CIDEP), can be used to determine reaction mechanisms.[3] In solid or solidlike matrixes, on the other hand, radical pairs and molecular triplet states can be measured and their spin-polarization patterns have been used to obtain structural information in photosynthetic reaction centers[4] and donor−acceptor model compounds.[2] The spin polarization occurs as a result of the correlation of the electron spins in the paramagnetic excited states, or photoproducts generated by the light excitation. For example, when a radical pair is generated rapidly from the excited singlet state of a molecule, the spin correlation present in the singlet state is retained in the radical pair. Because of this dependence of the spin polarization on the nature of the precursors to a given reaction intermediate, the pathway of the reaction can be deduced by analyzing the spin-polarization patterns and their time developments.

When the ground state is paramagnetic, light-induced processes can generate systems with more than two interacting spins. Recently, there has been considerable interest such systems.[5−11] For example, the polarization of a stable radical through its interaction with a light-induced radical pair has been studied in bacterial photosynthetic reaction centers[12−14] and the radical−triplet pair mechanism of CIDEP has been investigated by several authors.[15−17] The light-induced EPR signals from complexes with a photoexcitable species such as a porphyrin or fullerene with attached nitroxide spin labels have revealed doublet, quartet, and quintet components,[18,19] which could be distinguished by their different nutation frequencies.[9]

In a previous study, we reported spin-polarization patterns for a copper porphyrin-free base porphyrin heterodimer.[20] The structure and the energy transfer scheme of the dimer are shown in Figure 1 and as can be seen, selective excitation of either half eventually leads to population of the excited state labeled $^{2,4}[^2S_0\cdots{}^3T_1]$, which represents a triplet excitation of the free base porphyrin (H_2P) part in the dimer. This state is a weakly coupled triplet−doublet pair because of the interaction of the triplet spin with the Cu(II) doublet ground state. The dependence of the spin polarization on the excitation wavelength confirms that energy transfer from the copper porphyrin half of the dimer to the free base half occurs via the trip−quartet and/or trip−doublet states of the copper porphyrin.

* Corresponding authors. (Art van der Est) E-mail: avde@brocku.ca. FAX: 905-682-9020. (Motoko Asano-Someda) E-mail: motoko@chem.titech.ac.jp. FAX: +81-3-5734-2655.

† Department of Chemistry, Brock University.

‡ Department of Chemistry, Tokyo Institute of Technology.

10.1021/jp025561m CCC: $22.00
Published on Web 08/27/2002

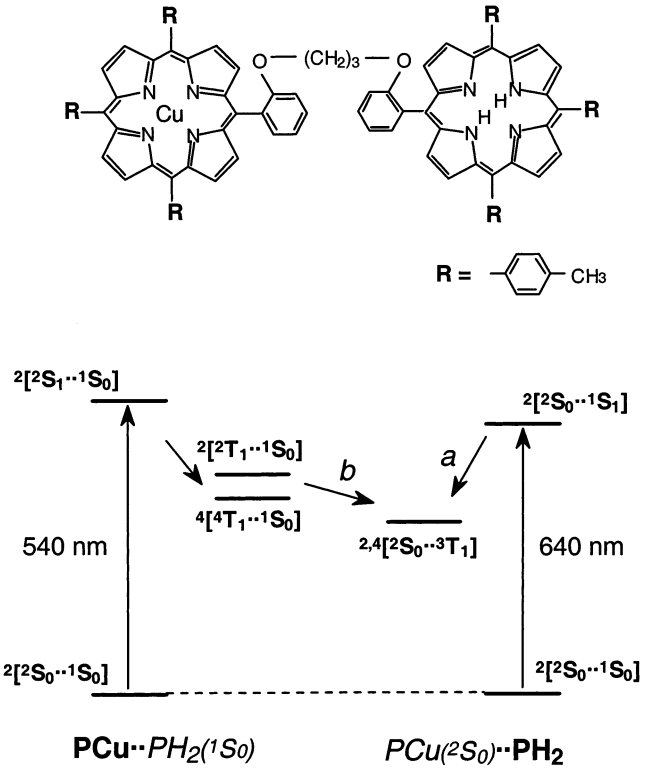

Figure 1. The molecular structure of $Cu-C_3-H_2$ and an energy diagram of the dimer constituents. The transition wavelengths indicated in the figure are those used to selectively excite the two halves of the dimer, PCu and PH_2. The states are labeled according to the electronic state of each half of the dimer and the total spin multiplicity. The two pathways leading to population of the triplet state of PH_2 are labeled (a) ISC within the PH_2 moiety and (b) energy transfer from the trip-quartet state of PCu. Note that the figure is meant to give only a qualitative picture and the relative energies are not to scale.

The characteristic polarization patterns observed for the two pathways in the dimer were explained qualitatively as resulting from the spin selectivity of the population and depopulation of the $^{2,4}[^2S_0\cdots{}^3T_1]$ state. The two pathways were assumed to produce different initial population distributions of the spin sublevels and it was postulated that subsequent spin-selective depopulation occurred according to the doublet character of the spin system. Apart from its interesting photophysics, this dimer system provides a framework within which we can discuss features of the spin-polarization patterns of correlated, coupled triplet−doublet pairs in a general way. Two critical features of the qualitative model presented in the previous work[20] are the strength of the spin−spin coupling and the postulated spin-selective depopulation. To test our model and study the properties of triplet−doublet pairs in general, we have examined spin-polarized EPR signals of the dimer in liquid crystalline solvents at two microwave frequencies. The data allow us to analyze the time-evolution of the spin-polarization patterns quantitatively and examine their dependence on the Zeeman energy. Here, we present a general description of weakly coupled triplet−doublet pairs, which is consistent with most of the features of the dimer including the time, orientation and microwave frequency dependence of the polarization patterns. Further, we will use the model to consider details of the expected polarization patterns in the different generation pathways and discuss the possible influence of spin relaxation.

2. Experimental Section

The free base-copper hybrid dimer $Cu-C_3-H_2$ was synthesized as described previously.[21,22] EPR samples were prepared by dissolving the dimer in the liquid crystalline solvent, E7 (BDH) to a concentration of 10^{-4} M. The solutions were placed in suprasil EPR sample tubes (3 mm o.d.) and were degassed by several freeze−pump−thaw cycles and then sealed under vacuum.

The samples were ordered macroscopically by freezing from the nematic phase in the magnetic field of the spectrometer. The frozen samples were then measured with the director parallel to the field, rotated by 90°, and measured again with the director perpendicular to the field.

The transient EPR (TREPR) measurements were performed at X-band (9 GHz) and K-band (24 GHz) using a setup described previously.[23,24] Reliable optical excitation at different wavelengths was achieved using a Nd:YAG pumped optical parametric oscillator described in detail elsewhere.[20]

3. Experimental Results

As shown in Figure 1, excitation with 640 nm results in a triplet excitation of the free base half of the dimer via intersystem crossing, while excitation at 540 nm gives the same final excited state via energy transfer from the copper porphyrin. Together with the doublet ground state of the Cu(II) metal atom in the other half of the dimer, this state ($^{2,4}[^2S_0\cdots{}^3T_1]$ in Figure 1) constitutes a weakly coupled triplet−doublet pair[20,21] which is deduced to be the main component of all the observed spectra in this work.

3.1. X-Band Spectra in a Liquid Crystalline Solvent: Orientation and Wavelength Dependence. X-band TREPR spectra of $Cu-C_3-H_2$ in the liquid crystal (LC) E7 are presented in Figure 2. The left side of Figure 2 (part A) shows spectra taken with the LC director parallel to the external field, while the right side (part B) shows corresponding spectra with the director perpendicular to the field. The spectra in both parts of the figure were taken at 80 K with excitation at 640 nm (top) and 540 nm (bottom). The labels X, X′, Y, Y′, Z, Z′ indicate the field positions where the *X*, *Y*, and *Z* canonical orientations of the triplet contribute to the overall spectrum. The time development of the polarization patterns is shown by the spectra taken at 1 μs (solid curves) and 4 μs (dashed curves). The details of the time development will be discussed below together with signal decay curves, taken at the field positions indicated by the arrows.

In Figure 2A, the polarization pattern corresponding to the X-canonical orientation of the triplet changes from *E*/*A* (*E* = emission; *A* = absorption) for λ_{ex}= 640 nm (top) to *A*/*E* for λ_{ex}= 540 nm (bottom). This difference between the two excitation wavelengths is a result of different populations of the spin states when the triplet−doublet pair is generated via the different pathways.[20,21] In both cases, the *X*- and *Y*-canonical orientations of the free base triplet dominate the spectra because the director of the LC is parallel to the field and the porphyrin plane is partially ordered such that its *X*- and *Y*-axes are parallel to both the director and the magnetic field.[25−27]

On the other hand, contributions from the *Z*-orientation dominate when the director is perpendicular to the field as seen in Figure 2B. The sign of the polarization at the *Z*-canonical orientation is *E*/*A* for both excitation wavelengths. By comparing the spectra with the two excitation wavelengths in Figure 2, it is apparent that the population distributions generated by the two pathways differ primarily for the *X*-canonical orientation.

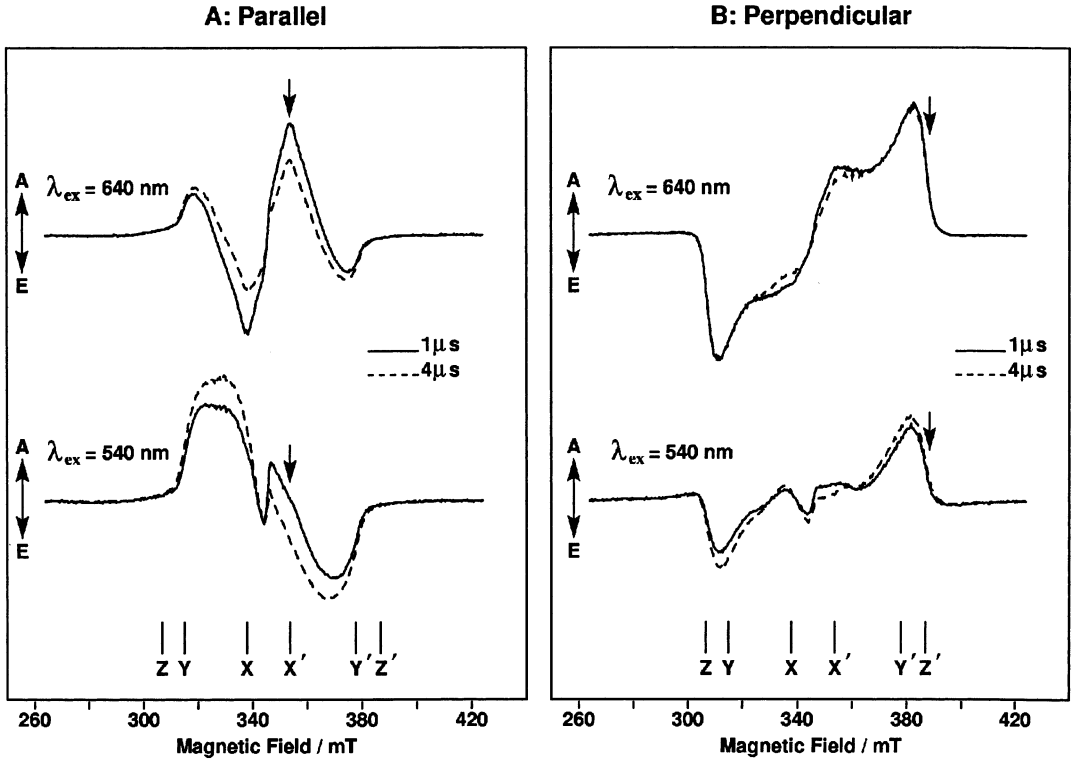

Figure 2. Spin polarization patterns of $Cu-C_3-H_2$ in the liquid crystal E7. All spectra are taken at X-band (9 GHz) and 80 K. The spectra represent the average signal in a time window 0.4 μs wide at either 1 μs (solid spectra) or 4 μs (dashed spectra) after the laser flash. Top: spectra obtained with an excitation wavelength $\lambda_{ex} = 640$ nm. Bottom: $\lambda_{ex} = 540$ nm. The labels X, Y, and Z and X', Y', and Z' indicate the positions of features originating from molecules with the *X*-, *Y*-, or *Z*-axis of the PH_2 zfs tensor parallel to the field. A: The director oriented parallel to the magnetic field. The arrows indicate the position at which the transients labeled X′ in the top part of Figure 3 were taken. B: The director oriented perpendicular to the field. The arrows show the field positions corresponding to the transients labeled Z′ in the bottom part of Figure 3.

3.2. Time Dependence of the X-band TREPR Spectra. The time development of the TREPR spectra of $Cu-C_3-H_2$ is complex, with both the rise and decay of the spectra being dependent on the excitation wavelength. This is demonstrated in Figure 2 by the polarization patterns taken at 1 μs (solid curves) and 4 μs (dashed curves) for two orientations of the sample. In Figure 2A, it can be seen that when the triplet−doublet pair, $^{2,4}[^2S_0 \cdots ^3T_1]$, is formed by ISC ($\lambda_{ex} = 640$ nm, Figure 2A top), the overall amplitude of the spectrum decreases between 1 and 4 μs. On the other hand, when the same state is generated by the energy transfer pathway ($\lambda_{ex} = 540$ nm, Figure 2A bottom), the signal intensity increases during the time window between 1 and 4 μs.

A similar effect can be seen in the spectra taken with the director perpendicular to the field (Figure 2B), although it is not as pronounced as in Figure 2A. Again, the signal decreases between 1 and 4 μs after the laser flash for the ISC pathway (Figure 2B top), while for the energy transfer pathway (Figure 2B, bottom) it increases in the same time range.

Comparison of Figures 2A and 2B reveals that although the overall behavior is the same (i.e., a signal decrease for ISC and a signal increase for energy transfer), there is a clear difference in the orientation dependence of the respective increase or decrease for the two pathways. In the case of the ISC pathway with $\lambda_{ex} = 640$ nm, the rate of decay depends significantly on the orientation. The largest decrease is seen for the *X*-orientation (Figure 2A, top) and smallest for the *Z*-orientation (Figure 2B top). The *A*/*E* pattern corresponding *Y*-orientation (positions Y and Y′, Figure 2A, top) actually shows a slight apparent increase due to overlapping signal contributions with differing signs and decay rates. In contrast, for the energy transfer pathway ($\lambda_{ex} =$ 540 nm, bottom spectra in Figures 2A and 2B) the increase in the intensity of the spectrum between 1 and 4 μs is roughly the same for all three canonical orientations.

3.3. Kinetics Traces. Figure 3 shows kinetic traces corresponding to the positions marked with arrows in Figure 2. These traces represent the rise and decay of the spin polarization at the *X*- and *Z*-canonical orientations. The solid curves are the experimental data, and the dashed and dotted curves are fits, which will be described in more detail later. Note that while excitation at 640 nm is almost perfectly selective for the free base porphyrin ($^2[^2S_0 \cdots ^1S_1]$ Figure 1, right side), irradiation at 540 nm is only partially selective for the copper porphyrin ($^2[^2S_1 \cdot \cdot \cdot ^1S_0]$ Figure 1, left side), i.e., some excitation of the free base also occurs at 540 nm. (See absorption spectra in ref 20).

In the case of the *X*-orientation (Figure 3 top), the signal with $\lambda_{ex} = 640$ nm rises with the response time of the spectrometer and decays biexponentially with the faster component dominating. On the other hand, the behavior of the signal with $\lambda_{ex} =$ 540 nm is more complicated. This is due mostly to the fact that we have contributions from both pathways, i.e., we also excite the free base to some extent and have an ISC contribution. The observed time trace can be ascribed to a superposition of the two signals, which are shown by the dotted curves and have been obtained from a fit of the transient (the details of the fitting procedure is discussed in more detail below). The positive contribution is from the ISC process and has a fast rise time. On the other hand, the negative component from the energy transfer pathway rises with a time constant, which is considerably slower than the rise time of the spectrometer. These observations are also consistent with Figure 2A, where the spectrum with $\lambda_{ex} = 640$ nm rises promptly and decays quickly whereas the spectrum with $\lambda_{ex} = 540$ nm rises slowly.

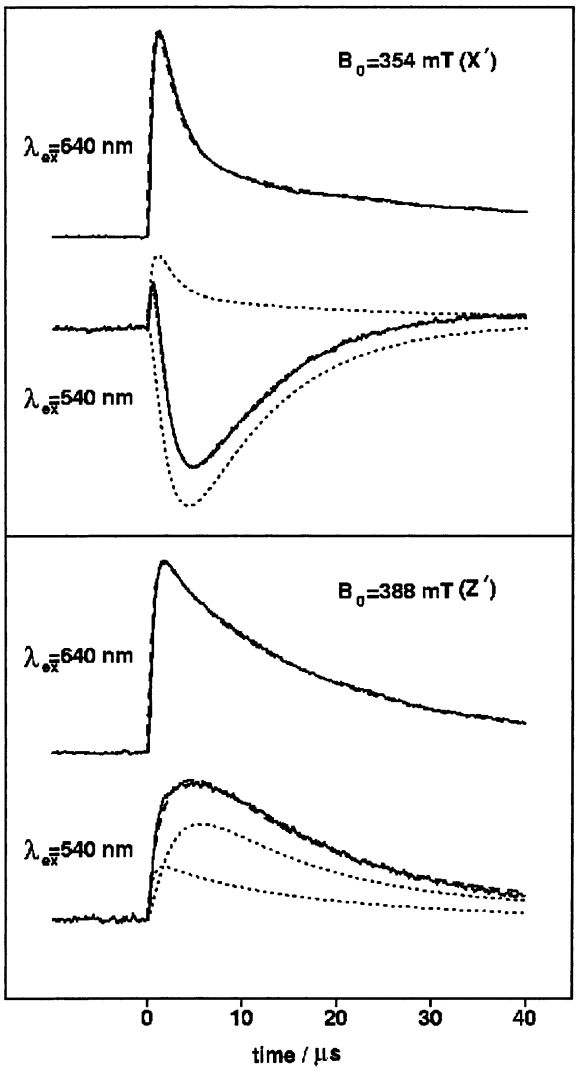

Figure 3. Time traces taken at the field positions indicated by the arrows in Figure 2. The dotted curves are fits to the experimental data (solid curves). With $\lambda_{ex} = 640$ nm the fitted curve is a biexponential decay with the following lifetimes and amplitude ratios. X′: $\tau_1 = 18$ μs, 25%; $\tau_2 = 1.8$ μs, 75%. Z′: $\tau_1 = 18.3$ μs, 84%; $\tau_2 = 3.0$ μs, 16%. With $\lambda_{ex} = 540$ nm the traces have been fitted by adding the result of the fit at $\lambda_{ex} = 640$ nm to a curve with the following rise and decay lifetimes. X′: $\tau_{rise} = 1.8$ μs, $\tau_{decay} = 10$ μs. Z′: $\tau_{rise} = 2.4$ μs, $\tau_{decay} = 14$ μs decay. The contributions to the fitted curve are shown individually in the figure.

For the *Z*-orientation (Figure 3 bottom), the signal decay with $\lambda_{ex} = 640$ nm is much slower compared to that for the *X*-orientation (Figure 3 top) although the rise time is the same as that for the *X*-orientation. Similar to the *X*-orientation, the signal with $\lambda_{ex} = 540$ nm can be considered as a superposition of two positive contributions associated with the two pathways. Again, the component associated with the energy transfer has a slow rise, while the contribution from ISC has a fast rise. These transient traces are consistent with the behavior observed in Figure 2B.

From the transients, we can confirm (i) Excitation at $\lambda_{ex} = 540$ nm leads to a signal component that rises with a comparatively slow time constant, which does not depend strongly on the molecular orientation. (ii) The decay of the ISC component is strongly orientation dependent and is fastest for the *X*-orientation and slowest for the *Z*-orientation.

3.4. K-Band Spectra in a Liquid Crystal Solvent: Microwave Frequency Dependence. Although the main features of the spectra in Figures 2A and 2B appear at field positions corresponding to those of the unperturbed triplet state, there are also additional features in the center of the spectrum, which have no triplet state counterpart. These features are seen most clearly with excitation at 540 nm, (Figures 2A and 2B, bottom) and are consistent with previous observations in frozen toluene solution.[20] These features have been tentatively assigned to conformations of the dimer in which the coupling between the triplet and doublet is strong, however this assignment is not yet firmly established. The microwave frequency dependence of the spectra provides additional information on which the assignments can be based because the Cu doublet has a considerable g-anisotropy. To this end, we have carried out K-band measurements.

In Figure 4 spectra measured at a microwave frequency of 9 GHz (X-band) and 24 GHz (K-band) are compared. The spectra have been taken at 50 K and the solid curves are the K-band data while the dashed curves are the X-band results. The latter are similar to the corresponding spectra in Figures 2A and 2B taken at 80 K. In Figure 4, the spectra are plotted such that the field position corresponding to $g = 2.0023$ and the total width in mT are the same for both frequency bands.

As can be seen in the upper parts of Figures 4A and 4B, only minor differences between the two frequency bands are observed when excitation with 640 nm is used. This observation provides a support for our assignment of the main component of the spectra to the state $^{2,4}[^2S_0 \cdots ^3T_1]$ with weak coupling between the doublet $^2S_0$ and the triplet $^3T_1$ (see details in the Discussion section). On the other hand, when excitation at 540 nm is used (Figures 4A and 4B, bottom) significant differences in the spectra taken at the two microwave frequencies become apparent. In particular, the relatively narrow emission/absorption feature at the center of the spectra shows a larger separation at K-band. This is seen most clearly for the parallel orientation in the lower part of Figure 4A. As we will show below, the observed behavior is consistent with that of a quartet and a doublet state and supports our assignment of the narrow features to conformations of the molecule in which the coupling between the free base triplet and Cu doublet is strong.

4. Theoretical Model

To provide a basis for discussing the various features of the experimental spectra, we present a general theoretical description of coupled triplet−doublet spin pairs including a simple model for their dynamics. While similar descriptions for weakly coupled doublet−doublet pairs have been discussed by several authors and are well established as the CCRP model first introduced by Closs et al.,[28] there are relatively few examples for weakly coupled triplet−doublet pairs with a fixed geometry. First, we will discuss the energy levels and transition frequencies of the system as a function of the coupling between the $S = {}^1/_2$ and $S = 1$ spins. Then we present the expected spin-polarization patterns, with different initial population distributions resulting from different possible pathways. The model will then be applied to the analysis of our porphyrin dimer system.

4.1. Coupled Triplet−Doublet Spin Pairs. The behavior of any coupled spin system depends critically on the strength of the coupling. In the coupled triplet−doublet system, the limiting cases of weak coupling and strong coupling can be easily treated analytically. In both instances, there are six eigenstates, which can be described using either a triplet−doublet or quartet−doublet basis. Figures 5A and 5B show energy level diagrams and stick spectra for the two cases. The details of the energies and transition frequencies are given in Appendix 1 along with general expressions for the wave functions and eigenvalues.

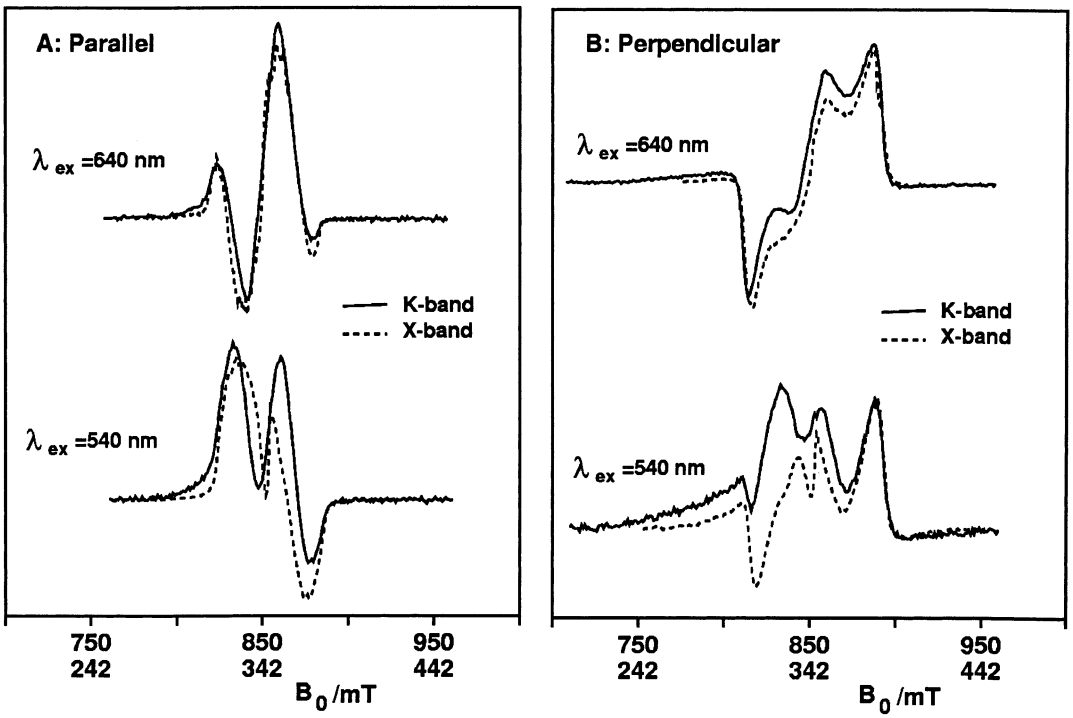

Figure 4. Microwave frequency/ magnetic field dependence of the spin-polarization patterns of $Cu-C_3-H_2$ in the liquid crystal E7. A: Liquid crystal director oriented parallel to the field. B: Liquid crystal director oriented perpendicular to the field. Solid spectra: X-band (9 GHz). Dashed spectra: K-band (24 GHz). The spectra have been superimposed such that the total spectra width in mT and field position corresponding to $g = 2.0023$ are the same for both frequency bands. The excitation wavelength is as shown. Temperature: 50 K. Time window: 0.2−0.3 μs (K-band), 1−2 μs (X-band). Different time windows have been used to take the faster response time of the K-band spectrometer into account.

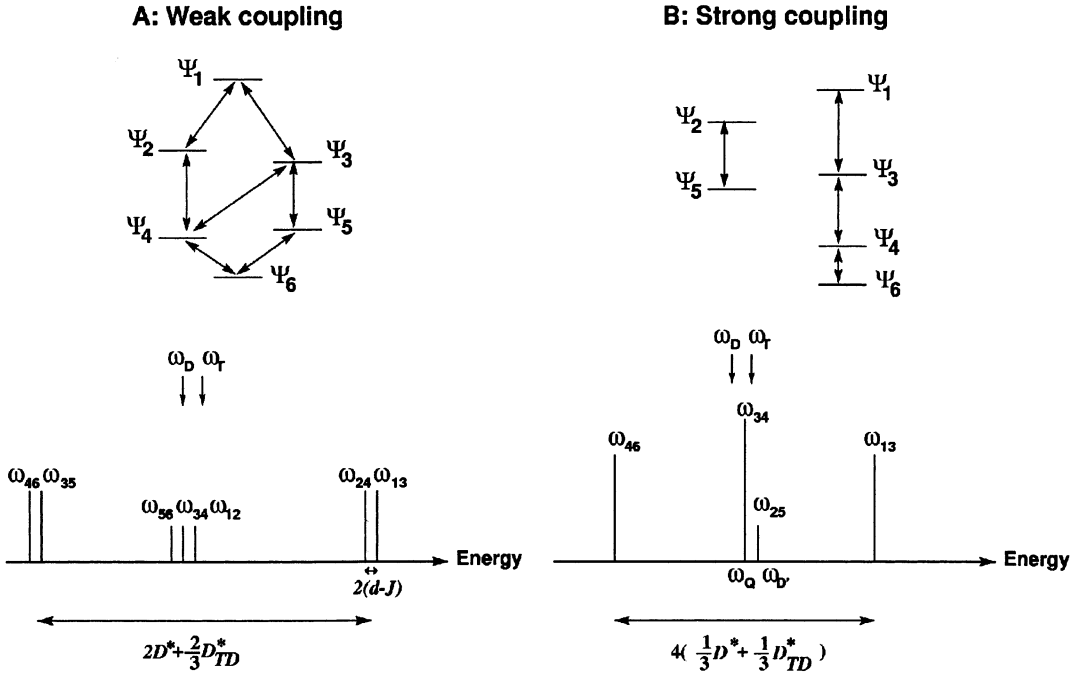

Figure 5. Energy level diagram and stick spectra of a coupled triplet doublet spin pair. A: Weak coupling. B: Strong coupling. The expressions for the energy levels and transitions frequencies are given in Appendix 1. The resonance frequencies of the triplet and doublet spins have been chosen such that $\omega_T > \omega_D$ as indicated by the arrows. The spin−spin coupling between the triplet and doublet is taken as $d > J > 0$. The heights of the lines in the stick spectrum represent the transition probabilities.

In the case of weak coupling, the wave functions are approximately product states of the triplet and doublet. As can be seen in Figure 5A, there are seven allowed EPR transitions. Four of these are associated primarily with the triplet spin and three are doublet transitions. (Note, however, that this assignment of the transitions to individual spins is only strictly valid in the limit of zero coupling.) The corresponding stick spectrum is shown in the bottom part of Figure 5A. The two pairs of the triplet transitions with frequencies ω_{13}, ω_{24}, ω_{35}, and ω_{46} have a splitting of $(\omega_{13} - \omega_{24}) = (\omega_{35} - \omega_{46}) = 2(d-J)$ in each pair. The doublet transitions ω_{12}, ω_{34}, and ω_{56} are centered at the resonance frequency of the doublet and have the same splitting as the pairs of triplet transitions. The total spectral width $(2D^* + {}^2/_3D^*_{TD})$ is slightly wider than the corresponding

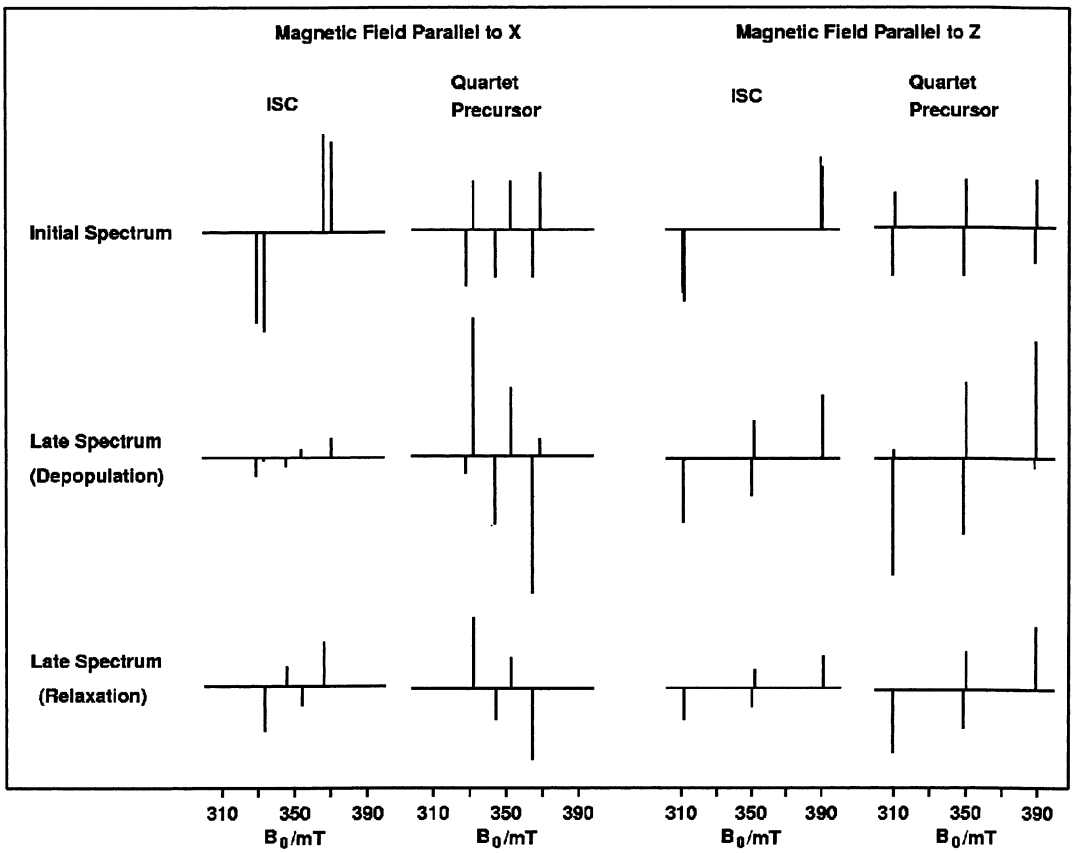

Figure 6. Stick spectra showing the expected polarization of the weakly coupled triplet doublet pair formed by a triplet excitation of PH_2 (i.e., the state labeled $^{2,4}[^2S_0\cdots{}^3T_1]$ in Figure 1). The spectra are calculated for either the *X*-axis or the *Z*-axis of the PH_2 zfs tensor oriented parallel to the field (B_0) as indicated. The patterns expected from the two pathways, ISC (path a in Figure 1) and energy transfer from a quartet precursor (path b in Figure 1), are shown. From top to bottom, they indicate the initial polarization (top), the effect of selective depopulation (middle) and the effect of flip-flop spin relaxation (bottom). The parameters are the same as used for the simulations in Figure 7 except that the g-factor of the doublet has been placed at 2.0023 and the hyperfine couplings have been ignored in the interest of clarity.

original triplet ($2D^*$). As a result, the powder averaged spectrum for a random distribution of orientations relative to the field is slightly broader than the superposition of the triplet and doublet spectra alone.

As the strength of the coupling increases, the degree of the triplet−doublet mixing increases. The transition probabilities associated with the triplet transitions become unequal and one of them becomes increasingly forbidden. The situation is similar for the three doublet transitions with the two outer lines losing intensities as the coupling increases. In addition, the frequencies of these transitions, i.e., ω_{12}, ω_{24}, ω_{56}, and ω_{35} are shifted to much higher or lower values as their intensities become weak. As a consequence, these four transitions disappear from the spectrum in the strong coupling limit. In contrast, the transition between states 2 and 5, which is forbidden in the weak coupling, becomes allowed. When the coupling is sufficiently strong, only four transitions are allowed as described in Appendix 1(eqs A1.17 and A1.18).

Figure 5B shows energy levels and stick spectra of the strong coupling case. Three of the transitions correspond to the trip−quartet manifold while the fourth is a trip-doublet transition. The total width of the spectrum is narrower than the original triplet component, as has been observed in strongly coupled systems.[29]

4.2. Expected Spin-Polarization in Weakly Coupled Triplet−Doublet Pairs. We now consider the expected spin polarization in weakly coupled triplet−doublet pairs. A complete discussion would include the motion of the spin system under a time dependent Hamiltonian from a given set of initial conditions. However, to grasp basic features of such systems, it is sufficient to deal with the initial populations resulting from different excitation pathways and the evolution of the population due to various relaxation mechanisms along with their orientation dependence.

4.2.1. Initial Spectra. Here we consider two situations for the population pathways: (i) spin−orbit intersystem crossing within the species carrying the triplet (ii) energy transfer from a quartet or doublet precursor. In case (i), we assume that the relative rates of ISC follow $P_x > P_y > P_z$, and in case (ii) we assume population according to the spin-quantum number of the precursor, which has its spin states equally populated. Although, these pathways correspond to the situation in the Cu−C_3−H_2 dimer (Figure 1), our purpose is to describe the system generally and we do not need to make any assumptions about the specific system being considered. Indeed, the two cases represent the two general situations in which the spin selectivity of the population pathway is governed by interactions internal to the molecule (case i) or interaction with the external field (case ii).

Figure 6 shows the expected stick spectra for the weak-coupling case for the two population pathways. The spectra are calculated for the magnetic field oriented along the *X*-axis of the triplet ZFS tensor ($B_0||X$). Initially, for the ISC case only lines associated with the triplet state are observed (Figure 6, columns 1 and 3, top row). This is because both orientations of the doublet spin are equally probable and states that differ only by a flip of the doublet spin will have equal population. Note

that within each of the pairs of triplet transitions both lines have the same sign.

In contrast, the initial spectra observed with a quartet precursor (Figure 6 columns 2 and 4, top row), consist of three antiphase doublets. The two outer anti-phase doublets correspond to triplet transitions, whereas the middle one is from the doublet. In general, the lines of the stick spectrum will be inhomogeneously broadened, primarily due to unresolved hyperfine couplings, and the line width will be larger than or comparable to the splitting. Under these conditions, the lines will add in the ISC case but cancel in the quartet precursor case. Accordingly, the initial spectrum should closely resemble that of the original triplet in the ISC case but will be very weak with a quartet precursor.

4.2.2. Late Spectra. After the initial population of the weakly coupled triplet−doublet states, we consider two possible mechanisms that would change the spin distribution of the system. These two mechanisms reflect characteristic properties of the triplet−doublet system. One is selective depopulation of the spin-states with doublet character, i.e., Ψ_2, Ψ_3, Ψ_4, and Ψ_5, as we have proposed previously.[20] The other is a flip-flop relaxation mechanism between states with the same value of m_z, i.e., $\Psi_2 \leftrightarrow \Psi_3$ and $\Psi_4 \leftrightarrow \Psi_5$. Fluctuations of dipolar-dipolar coupling and/or exchange coupling can cause a flip-flop of the two spins, leading to equalization of the population between spin states with the same quantum number, m_z. The expected spectra for both mechanisms are presented in the middle and bottom rows of Figure 6.

In the case of ISC, both mechanisms lead to a decrease in the intensities of the lines associated with the triplet transitions (Figure 6, columns 1 and 3, middle and bottom rows) while in the center of the spectra, the copper doublet transitions appear with antiphase polarization. Thus, spin polarization associated with the doublet is expected to increase with time. However, the intensity of these contributions will be weak due to the cancelation effect discussed above. In contrast, for the quartet precursor (Figure 6, columns 2 and 4, middle and bottom rows) the two mechanisms remove the cancellation effect for the triplet transitions while it remains intact for the doublet (Cu) transitions. Thus, we expect the triplet spectrum to increase in intensity, as the states of doublet character are depopulated or flip-flop relaxation takes place.

In short, Figure 6 shows that both mechanisms have a similar effect on the time development of the spectra. However, when the triplet−doublet pair is formed by ISC they lead to a decrease in intensity whereas when the pair is formed from a quartet precursor they cause the signal to increase in intensity as time develops.

4.2.3. Orientation Dependence. The orientation dependence of the initial and late spectra can also be seen in Figure 6 by comparing the left side of the figure, which corresponds to B_0//X, and the right side which shows spectra for B_0//Z. From this comparison, it is apparent that the intensity of the late spectrum is weak for B_0//X in the ISC case (Figure 6, column 1, lower two spectra). This is because the ISC mechanism selectively populates states $\Psi_2-\Psi_4$ for this orientation and it is these states, which are affected most by the selective depopulation and flip-flop mechanisms. Whereas, with B_0//Z and ISC (Figure 6, column 3, lower two spectra), the effect of the two mechanisms is much less because $\Psi_1-\Psi_6$ are populated to a large extent for this orientation. In contrast to the ISC case, when the system is populated from a quartet precursor (Figures 6), the intensity of the late spectrum is roughly the same for both orientations. This is reasonable since both the initial population and the decay mechanisms depend only on the quartet and doublet character of the spin states, which are not strongly orientation dependent. As a consequence, the decay of the spin polarization for the ISC case is orientation dependent while the rise of the spectra for the energy transfer case is less orientation dependent.

5. Analysis and Discussion

Based on the above theoretical considerations, we now discuss our experimental results in the framework of triplet−doublet pairs.

5.1. Microwave Frequency Dependence. The most important conclusion we can confirm from Figure 4 is that the main component of the spectra arises from a weakly coupled triplet−doublet species. This confirmation comes from the close correspondence of the triplet-like spectra measured at two different microwave frequencies, demonstrating that the zero-field splitting (zfs) of the triplet dominates the EPR spectra. Thus, the perturbation of the original triplet by the coupling with the doublet is small. (see Figure 5A and Appendix 1, eq A1.16).

Another important piece of information, which can be obtained from Figure 4 is the assignment of the features, which appear in the center of the spectrum and show a significant microwave frequency dependence. Our initial assignment was to a strongly coupled doublet−triplet pair in conformations of the dimer in which the two porphyrins are in close proximity to one another. This assignment[20] was based primarily on the estimated g-values of the quartet and doublet transitions (eqs A1.17 and A1.18). However, the stick spectra in Figures 5 and 6 show that the doublet transitions of the weakly coupled triplet−doublet pair also contribute in this region and it is possible that they are responsible for these contributions. These two possible assignments can be distinguished by their magnetic field dependences relative to the features associated primarily with the free base triplet. Figure 4 shows that the *E*/*A* features near the middle of the spectrum become broader at K-band (24 GHz) compared to X-band (9 GHz) and the components are shifted in opposite directions relative to the middle of the triplet spectrum as the microwave frequency increases.

Since the splitting between the triplet transitions of the weakly coupled triplet−doublet pair are not field dependent except at very low field, they provide a reference point against which the shift of the spectral features with changes in the field can be measured. The center of the triplet powder spectrum corresponds to $g_T = \hbar\omega_T/\beta B_0$ and for the free base porphyrin it is close to free electron g-factor, g_e. The principal *g*-values of the copper doublet, on the other hand, are larger than g_e and features associated with the doublet transitions in a weakly coupled pair will appear downfield from the center of the triplet spectrum (eq. A1.15). Thus, if the emissive and absorptive features in the center of the spectrum are from the copper doublet, both the features should move downfield relative to the center of the triplet spectrum with increasing microwave frequency. However, this does not agree with what is observed in the dimer (Figure 4).

On the other hand, as can be seen in eqs A1.17 and A1.18), the $m_z = \pm^1/_2$ transitions of the quartet and doublet states of a strongly coupled doublet−triplet pair will lie on opposite sides of g_T. If the *E*/*A* features are from a strongly coupled species, they will move in opposite directions relative to field position corresponding to g_T. This is consistent with Figure 4 and confirms our previous assignment that the features are from the quartet and doublet transitions in conformations of the dimer in which the coupling strong.

5.2. Kinetics. We now examine the time traces (Figure 3) in more detail to estimate the rate of the spin-selective depopulation or relaxation. In keeping with our treatment of the spectra in which only changes in the populations of the states were considered, we restrict ourselves to an empirical analysis and will not explicitly consider coherent motion of the spin system. The analysis of the kinetics is complicated by the fact that the datasets contain overlapping contributions from different orientations and conformations of the complex. Thus, we use only the selected transients shown in Figure 3, which correspond to the weakly coupled conformations at the *X*- and *Z*-canonical orientations. We begin by fitting the traces taken with $\lambda_{ex} =$ 640 nm because this excitation is completely selective for the ISC pathway. Inspection of the traces shows that they are biexponential and have a rise time of ~500 ns due to the narrow bandwidth of the resonator (cf. Figure 3, top trace). Therefore we have fit the transients using a biexponential decay function convoluted with the response function of the spectrometer. As shown in Figure 3, the curves marked $\lambda_{ex} = 640$ nm can be fitted well and components with decay times of $\tau \approx 2$ μs and $\tau \approx 20$ μs are found at both field positions. The trace corresponding to the *X* canonical orientation (Figure 3 top, marked *X*′) is dominated by the faster component while the trace marked *Z*′ is dominated by the slower component.

On the other hand, excitation of the dimer at $\lambda_{ex} = 540$ nm predominantly leads to excitation of the copper porphyrin and energy transfer to the free base. However, as described in the Results section, it is not completely selective and we expect a minor contribution from the ISC pathway due to direct excitation of the free base. This is most evident in the trace at $\lambda_{ex} = 540$ nm for *X*′ (Figure 3 top). As can be seen in Figure 3, excellent agreement between the experimental transients at $\lambda_{ex} = 540$ nm and their fits are obtained for both the *X*′ and the *Z*′ orientation by adding a component with a slow rise time to the decay curve for the ISC contribution, which was obtained from the fitting procedure with $\lambda_{ex} = 640$ nm.[30] The component found for the energy transfer pathway has a rise time of $\tau \approx 2$ μs and a single decay time of $\tau \approx 12$ μs for both traces of the *X*′ and *Z*′ orientations.

These results are consistent with the two models describing either an equalization or a depletion of the populations of the $m_z = \pm 1/2$ sublevels. Both mechanisms will lead to a rise of the EPR signal when the spin system is populated from a quartet precursor and a decrease when the population is via ISC. If we assume that the fast component of the $\lambda_{ex} = 640$ nm decay is due to one or both of these mechanisms, it should dominate for the *X*′ orientation and be a minor component for the *Z*′ orientation as discussed in section 4.2.3. This is consistent with our observations. Further, the faster decay component of the decay should be the same as the rise time for $\lambda_{ex} = 540$ nm and the rise time should be orientation independent. Since both of these features are observed, we conclude that the depopulation/relaxation lifetime is reflected in the fast component of the $\lambda_{ex} = 640$ nm decay and the $\lambda_{ex} = 540$ nm rise time of $\tau \approx 2$ μs.

5.3. Simulations. Having shown that the kinetics is consistent with the proposed models, we now present simulations of the spin-polarized spectra. The simulations are based on the transition frequencies given in Appendix 1. The intensities of the transitions are then calculated from the populations of the states and the transition probabilities. Broadening due to unresolved hyperfine couplings and inhomogeneities are taken into account as a Gaussian line shape. The orientation of the dimer in the liquid crystalline environment is taken into account as described in Appendix 2.

The initial populations of the sates are calculated either via rates associated with the zero-field triplet states in the ISC case or by the quartet character of the states. The population is then allowed to change with time in accordance with either (i) a depopulation of the states according to their doublet character or (ii) an equalization of the populations of the $m_z = \pm 1/2$ sublevels with an exponential decay function. The two mechanisms produce very similar spectra with only minor differences. Therefore, only the first possibility, i.e., spin-selective depopulation will be presented.

Because of the large number of parameters, it is not feasible to obtain values for all of them by fitting the simulations to the experimental spectra. Fortunately, reasonable estimates for most of the parameters can be made from independent sources. The magnetic properties of the Cu porphyrin doublet (**g**-tensors and hyperfine coupling tensors) and free base porphyrin triplet state (zero-field splitting tensor and ISC population rates) are known from their monomer simulations and can be used also in the dimer. The spin−spin coupling between the triplet and doublet is difficult to determine accurately. However, using a model of the complex and the point dipole approximation, we estimate that the dipole−dipole coupling is on the order of −0.5 mT. The exchange coupling can be expected to of similar magnitude but its sign is not easily estimated.

The spectra also depend on the relative orientation of the magnetic tensors. Because the geometry is not known, we have made some simple but reasonable assumptions. First, we assume that principal axes of the free base triplet zfs tensor are aligned such that its *Z*-axis is normal to the porphyrin plane and the *X*- and *Y*-directions are through opposite pairs of nitrogen atoms. Next we assume that the two porphyrin rings are coplanar, i.e., the Cu **g**-tensor and the free base zfs tensor are parallel. Finally, we assume that the vector describing the dipolar coupling lies in the plane of both porphyrins at an angle of 45° to both the *X*- and *Y*-axes. To estimate the orientational distribution in the liquid crystal, we use parameters found for a porphyrin donor−acceptor complex with a similar structure.[27]

The results of the simulations are presented in Figure 7. Comparison of the simulations in Figure 7 with the corresponding experimental spectra in Figure 2 reveals that all of the essential features of the spin polarization are reproduced satisfactorily. In the energy transfer case (path b in Figure 1), we have assumed that the observed triplet−doublet pair is populated via the trip−quartet $^4[^4T_1 \cdots {}^1S_0]$. This is reasonable because the energy transfer occurs from the lowest lying excited state of the copper porphyrin and is consistent with the fast relaxation from the trip−doublet to the trip−quartet reported in other copper porphyrins.[31−33] It is important to note, however, that our assumption does not exclude the possibility of energy transfer via the trip−doublet, since the spin polarization generated via the trip−doublet and trip−quartet channels are complementary and cancel each other. Thus, if energy transfer from both the trip−doublet and trip−quartet occurs, we will observe only the excess polarization from the dominant pathway. The good agreement between the simulations (Figure 7, bottom spectra) and the experimental spectra (Figure 2, bottom spectra) clearly suggests that with $\lambda_{ex} = 540$ nm energy transfer occurs predominantly via the trip−quartet.

Moreover, the very different polarization patterns observed for the ISC population pathway (Figure 2, top spectra) are predicted properly. Comparison of Figures 7A and 7B with Figures 2A and 2B also show that the time development and

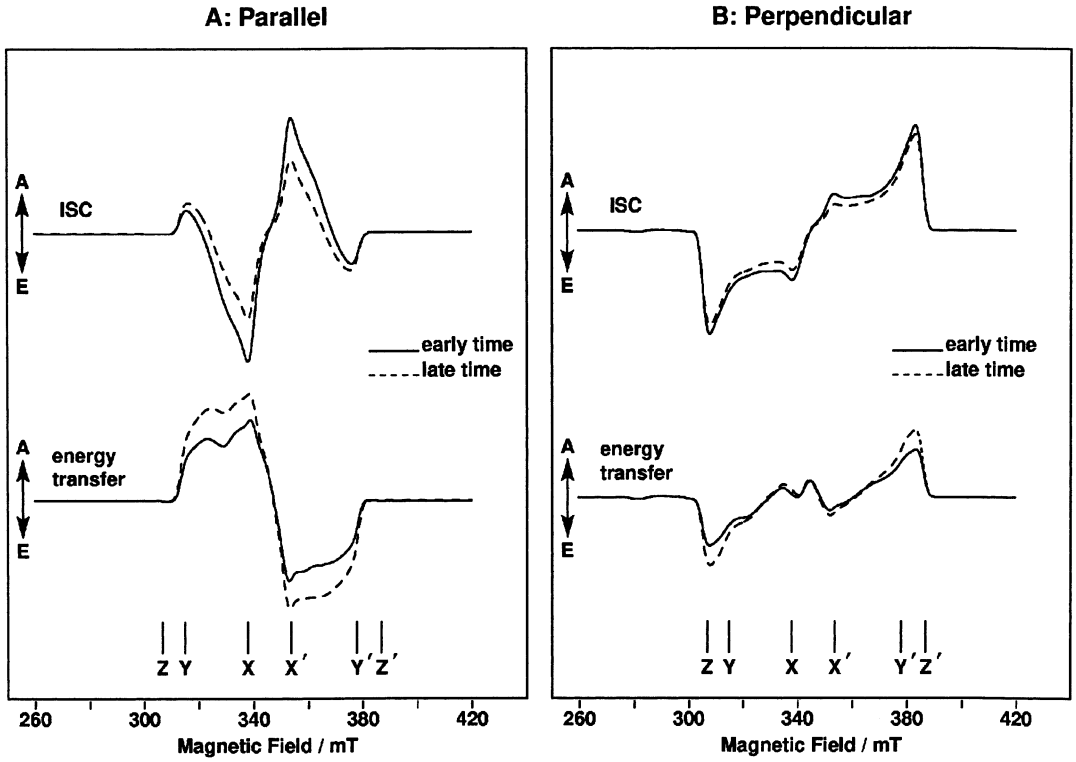

Figure 7. Simulations corresponding to the experimental spectra in Figure 2 The transition frequencies have been calculated using the expressions A1.14 and the orientation distribution has been calculated according to Appendix 2. The pathway by which the triplet is formed (ISC or energy transfer from a quartet precursor) is indicated and decay by spin-selective depopulation is assumed. The following parameters have been used: $g(^2\mathrm{Cu}) = \{2.053, 2.053, 2.193\}$, $g(^3\mathrm{PH_2})=\{2.0023, 2.0023, 2.0023\}$,$A(\mathrm{N}) = \{16, 16, 14\} \times 10^{-4}$ cm^{-1}, $A(\mathrm{Cu}) = \{33, 33, 203\} \times 10^{-4}$ cm^{-1}, $D_\mathrm{T} = 0.0375$ cm^{-1}, $E_\mathrm{T} = 0.0080$ cm^{-1}, $D_\mathrm{TD} = 0.0028$ cm^{-1}, $E_\mathrm{TD} = 0$, ISC population rates: P_x:P_y:$\mathrm{P}_z = 0.75$:0.25:0.00, $(T_{xx} - T_{yy}) = 0.0$, $T_{zz} = -4.0$. Early spectra $t/\tau = 0.5$; late spectra $t/\tau = 0.75$. The internal geometry used is discussed in the text.

dependence of the spectra on the liquid crystal orientation agree well with the experimental result. At present we cannot make a clear choice between the two possible mechanisms: spin-selective depopulation or flip-flop spin relaxation. The observed lifetime ($\tau \sim 2$ μs) associated with the process seems be closer to a spin-relaxation time than to a triplet state lifetime, which should correlate with spin-selective depopulation. The lifetime also displays a strong temperature dependence again in keeping with spin relaxation, which is usually very sensitive to temperature. However, this behavior does not rule out spin-selective depopulation. In the absence of experimental data, which clearly favor one process over another, the nature of the mechanism must be left as an open question.

Using the model outlined above, it is also possible to calculate the time dependence of the narrow spectral features assigned to strongly coupled conformations of the complex. However, such an analysis is complicated because these spectral features cannot be easily separated from the dominant weakly coupled triplet−doublet pair spectrum and the geometry of the conformations is not known. Moreover, spin relaxation due to modulation of the zeo-field splitting may also play contribute to the decay of the polarization of the quartet components for these conformations of the molecule. Therefore, we note only that in terms of the selective depopulation model the features belonging to the trip−doublet are predicted to decay more rapidly than those associated with the trip−quartet and that there is some evidence for such behavior in the spectra (see figure 6 of ref 20).

6. Conclusions

We have shown that the spin-polarization patterns from our porphyrin dimer can be well understood in the framework of a coupled triplet−doublet spin pair with different possible precursors and a spin-selective relaxation mechanism.

Especially by using partially ordered samples, the difference in the kinetic behavior of the polarization patterns was successively extracted for the two pathways as well as their differences in the orientation dependence. The good agreement between the experimental results and simulations, in Figures 2 and 7, shows that our model correctly predicts all major features of the observed spin polarization. In particular, the excitation wavelength dependence is explained quite naturally as a result of differences in the nature of the precursor.

The analysis of transients from the liquid crystal samples yields the same value of 2 μs, for both of the decay of the polarization in the ISC case and the rise of the polarization in the EnT case. Our model correctly predicts this behavior including the orientation dependence, although we are not yet able to clearly distinguish between the affect of the two proposed mechanisms. This result not only rationalizes the results in the present dimer system but also provides support for the contention that the model predicts the spin polarization of weakly coupled triplet and doublet pairs, generally.

Acknowledgment. This work was supported by the Natural Sciences and Engineering Research Council (NSERC) and by two Grants-In-Aid for Scientific Research from JSPS, no. 11694061 (International Joint Research, B), and no. 13640554.

Appendix 1

The spin Hamiltonian of a coupled triplet−doublet system is given by

$$H = \beta_e \mathbf{B}\cdot g_T \cdot \mathbf{S}_T + \beta_e \mathbf{B}\cdot g_D \cdot \mathbf{S}_D + \sum_i \mathbf{I}_{Ti}\cdot \mathbf{A}_{Ti}\cdot \mathbf{S}_T + \sum_i \mathbf{I}_{Di}\cdot \mathbf{A}_{Di}\cdot \mathbf{S}_D + \mathbf{S}_T\cdot \mathbf{D}_T\cdot \mathbf{S}_T - J_{TD}\left(\frac{1}{2} + 2\mathbf{S}_T\cdot \mathbf{S}_D\right) + \mathbf{S}_D\cdot \mathbf{D}_{TD}\cdot \mathbf{S}_T \quad \text{(A1.1)}$$

The six eigenstates are obtained by diagonalizing the Hamiltonian matrix in either a quartet−doublet or triplet−doublet basis. Here, we will use a quartet−doublet basis because it allows the quartet and doublet character of the eigenstates to be calculated more easily and it reflects the symmetry of the precursor when energy transfer from PCu takes place. In this basis the eigenstates at high field are

$$\Psi_1 = |Q_{3/2}\rangle$$

$$\Psi_2 = -\sin\theta|Q_{1/2}\rangle + \cos\theta|D_{1/2}\rangle$$

$$\Psi_3 = \cos\theta|Q_{1/2}\rangle + \sin\theta|D_{1/2}\rangle$$

$$\Psi_4 = \cos\phi|Q_{-1/2}\rangle + \sin\phi|D_{-1/2}\rangle$$

$$\Psi_5 = -\sin\phi|Q_{-1/2}\rangle + \cos\phi|D_{-1/2}\rangle$$

$$\Psi_6 = |Q_{-3/2}\rangle \quad \text{(A1.2)}$$

where

$$\tan 2\theta = \frac{2\sqrt{2}}{q_1}\left(\Delta\omega + \frac{1}{3}D^*\right), \quad \tan 2\phi = \frac{2\sqrt{2}}{q_2}\left(-\Delta\omega + \frac{1}{3}D^*\right) \quad \text{(A1.3)}$$

and

$$q_1 = -\Delta\omega - \frac{1}{3}D^* - \frac{3}{2}(d + 2J),$$

$$q_2 = \Delta\omega - \frac{1}{3}D^* - \frac{3}{2}(d + 2J) \quad \text{(A1.4)}$$

$$\Delta\omega = \frac{\hbar}{3}(\omega_T - \omega_D) \quad \text{(A1.5)}$$

$$\hbar\omega_T = g_{\text{eff}T}\beta_e B_0, \quad \hbar\omega_D = g_{\text{eff}D}\beta_e B_0 \quad \text{(A1.6)}$$

$$D^*(\theta_T,\phi_T) = D_T\left(\frac{3}{2}\cos^2\theta_T - \frac{1}{2}\right) + \frac{3}{2}E_T(\sin^2\theta_T\cos^2\phi_T - \sin^2\theta_T\sin^2\phi_T) \quad \text{(A1.7)}$$

$$D^*_{TD}(\theta_{TD},\phi_{TD}) = D_{TD}\left(\frac{3}{2}\cos^2\theta_{TD} - \frac{1}{2}\right) + \frac{3}{2}E_{TD}(\sin^2\theta_{TD}\cos^2\phi_{TD} - \sin^2\theta_{TD}\sin^2\phi_{TD}) \quad \text{(A1.8)}$$

$$d = \frac{2}{9}D^*_{TD}(\theta_{TD},\phi_{TD}) \quad \text{(A1.9)}$$

ω_T and ω_D are the resonance frequencies of the triplet and doublet, respectively and include the contribution from the local hyperfine fields. J is the exchange coupling between the triplet and doublet. D^* and d are the orientation dependent dipolar couplings within the triplet and between the doublet and triplet, respectively. The angles θ_{TD},ϕ_{TD} and θ_T,ϕ_T describe the orientation of the external field relative to the respective dipolar coupling tensors $\mathbf{D}_{TD}$ and $\mathbf{D}_T$. D_{TD}, E_{TD}, D_T, and E_T are the corresponding zero-field splitting parameters. When $\theta_{TD},\phi_{TD} = 0$ and $\theta_T,\phi_T = 0$, $D^* = D_T$ and $D_{TD}{}^* = D_{TD}$, respectively. The term for the dipolar coupling between the triplet and doublet in the Hamiltonian (eq A1.1) can be written using the operators $\mathbf{S}$ and $\mathbf{S_z}$ for the total spin and the parameter d in eq A1.9 as follows,

$$\mathbf{S}_D\cdot\mathbf{D}_{TD}\cdot\mathbf{S}_T = \frac{1}{2}d(3\mathbf{S}_z^2 - \mathbf{S}^2) \quad \text{(A1.10)}$$

The energies of the six eigenstates are given by

$$E_1 = \hbar\omega_T + \frac{1}{2}\omega_D + \frac{1}{3}D^* + \frac{3}{2}(d - J)$$

$$E_2 = \frac{1}{2}\left(\hbar\omega_T - \frac{1}{3}D^* - \frac{3}{2}d\right) - \Omega_1$$

$$E_3 = \frac{1}{2}\left(\hbar\omega_T - \frac{1}{3}D^* - \frac{3}{2}d\right) + \Omega_1$$

$$E_4 = \frac{1}{2}\left(-\hbar\omega_T - \frac{1}{3}D^* - \frac{3}{2}d\right) + \Omega_2$$

$$E_5 = \frac{1}{2}\left(-\hbar\omega_T - \frac{1}{3}D^* - \frac{3}{2}d\right) - \Omega_2$$

$$E_6 = -\hbar\omega_T - \frac{1}{2}\hbar\omega_D + \frac{1}{3}D^* + \frac{3}{2}(d - J) \quad \text{(A1.11)}$$

where and

$$\Omega_1 = \text{sign}(q_1)\frac{1}{2}\left\{{q_1}^2 + 8\left(\Delta\omega + \frac{1}{3}D^*\right)^2\right\}^{1/2} \quad \text{(A1.12)}$$

$$\Omega_2 = \text{sign}(q_2)\frac{1}{2}\left\{{q_2}^2 + 8\left(\Delta\omega - \frac{1}{3}D^*\right)^2\right\}^{1/2} \quad \text{(A1.13)}$$

The transition frequencies of the eight possible single quantum transitions are given by

$$\hbar\omega_{12} = \frac{\hbar}{2}(\omega_T + \omega_D) + \frac{1}{2}D^* + \frac{3}{2}\left(\frac{3}{2}d - J\right) + \Omega_1$$

$$\hbar\omega_{13} = \frac{\hbar}{2}(\omega_T + \omega_D) + \frac{1}{2}D^* + \frac{3}{2}\left(\frac{3}{2}d - J\right) - \Omega_1$$

$$\hbar\omega_{24} = \hbar\omega_T - \Omega_1 - \Omega_2$$

$$\hbar\omega_{34} = \hbar\omega_T + \Omega_1 - \Omega_2 \quad \text{(A1.14)}$$

$$\hbar\omega_{25} = \hbar\omega_T - \Omega_1 + \Omega_2$$

$$\hbar\omega_{35} = \hbar\omega_T + \Omega_1 + \Omega_2$$

$$\hbar\omega_{46} = \frac{\hbar}{2}(\omega_T + \omega_D) - \frac{1}{2}D^* - \frac{3}{2}\left(\frac{3}{2}d - J\right) + \Omega_2$$

$$\hbar\omega_{56} = \frac{\hbar}{2}(\omega_T + \omega_D) - \frac{1}{2}D^* - \frac{3}{2}\left(\frac{3}{2}d - J\right) - \Omega_2$$

In the limit of zero coupling between the triplet and doublet, the wave functions of the system become products of triplet and doublet basis states: $\Psi_1 = |T_{+1}\alpha\rangle$, $\Psi_2 = |T_{+1}\beta\rangle$, $\Psi_3 = |T_0\alpha\rangle$, $\Psi_4 = |T_0\beta\rangle$, $\Psi_5 = |T_{-1}\alpha\rangle$, and $\Psi_6 = |T_{-1}\beta\rangle$ and in the limit of infinite coupling, $\cos\theta = 1$, $\sin\theta = 0$, $\cos\phi = 1$, and $\sin\phi = 0$ in eq A1.2 and the wave functions become the quartet

and doublet basis states: $\Psi_1 = |Q_{3/2}\rangle$, $\Psi_2 = |D_{1/2}\rangle$, $\Psi_3 = |Q_{1/2}\rangle$, $\Psi_4 = |Q_{-1/2}\rangle$,$\Psi_5 = |D_{-/2}\rangle$, and $\Psi_6 = |Q_{-3/2}\rangle$.

In the case of weak coupling shown in Figure 5a, the transitions can be assigned to a flip of either the triplet or the doublet spin and the frequencies become doublet transitions:

$$\hbar\omega_{12} = \hbar\omega_D + 2d - 2J$$

$$\hbar\omega_{34} = \hbar\omega_D$$

$$\hbar\omega_{56} = \hbar\omega_D - 2d + 2J \qquad \text{(A1.15)}$$

and triplet transitions

$$\hbar\omega_{13} = \hbar\omega_T + D^* + \frac{5}{2}d - J$$

$$\hbar\omega_{24} = \hbar\omega_T + D^* + \frac{1}{2}d + J$$

$$\hbar\omega_{35} = \hbar\omega_T - D^* - \frac{1}{2}d - J$$

$$\hbar\omega_{46} = \hbar\omega_T - D^* - \frac{5}{2}d + J \qquad \text{(A1.16)}$$

In the strong coupling case the eigenstates become a doublet and quartet as shown in Figure 5b, the four allowed transitions are a doublet transition

$$\hbar\omega_{25} = \frac{\hbar}{3}(4\omega_T - \omega_D) \qquad \text{(A1.17)}$$

and three quartet transitions

$$\hbar\omega_{13} = \frac{\hbar}{3}(2\omega_T + \omega_D) + \frac{2}{3}D^* + \frac{2}{3}D^*_{TD}$$

$$\hbar\omega_{34} = \frac{\hbar}{3}(2\omega_T + \omega_D)$$

$$\hbar\omega_{46} = \frac{\hbar}{3}(2\omega_T + \omega_D) - \frac{2}{3}D^* - \frac{2}{3}D^*_{TD} \qquad \text{(A1.18)}$$

Appendix 2

To simulate spectra based on the transition frequencies given in Appendix 1, we take inhomogeneous broadening due to unresolved hyperfine couplings, magnetic field inhomogeneity, etc., into account with a Gaussian line shape,

$$I(\Omega,B_0) = I_0 \exp\{-(\omega_{ij} - \omega_0)^2/\Delta B\} \qquad \text{(A2.1)}$$

and integrate the line shape over all orientations of the molecule with respect to the external field:

$$I(B_0) = \int I(\Omega,B_0)P(\Omega)d\Omega \qquad \text{(A2.2)}$$

Here, Ω, represents the set of angles describing the orientation and $P(\Omega)$ is the orientational distribution function of the molecule in the liquid crystalline solvent. This distribution is determined by a potential energy surface:

$$P(\Omega) = \exp\{-U(\Omega)/kT\} \qquad \text{(A2.3)}$$

where $U(\Omega)$ is the potential energy of the solute as function of its orientation. The most general form for $U(\Omega)$ is the product of two second-rank tensors, one describing the solvent and the other the solute.[27,34] In a uniaxial liquid crystal, the tensor describing the solvent is axially symmetric and $U(\Omega)$ can be written as a function of the direction cosines between the molecular axes and the director of the liquid crystal:

$$U(\Omega) = T_{zz}\left(\frac{3}{2}l_{zZ}^2 - \frac{1}{2}\right) + \frac{T_{xx} - T_{yy}}{2}(l_{xZ} - l_{yZ}) \qquad \text{(A2.4)}$$

where l_{xZ}, l_{yZ}, and l_{zZ} are the direction cosines between the molecular x,y and z axes and the director, Z. T_{xx}, T_{yy}, and T_{zz} describe the strength of the tensorial solvent−solute interaction. With $U(\Omega)$ in such a form, the orientational distribution, $P(\Omega)$ of the solute is determined two parameters, T_{zz} and $(T_{xx} - T_{yy})/2$, and the directions of the axes x,y, and z in the molecule. In the frozen liquid crystal we also need to take into account the fact that the director can be rotated away from the magnetic field direction. For a given orientation of the director relative to the magnetic field, we define two space fixed axis systems: one with the magnetic field as its z-axis and the other with the director as its z-axis. The EPR signal $I(\Omega,B_0)$ depends on the relative orientation of the molecular and magnetic field axis systems, which can be expressed as an Euler matrix $\mathbf{R}_{IB}$. The direction cosines in eq A24 can then be obtained by calculating the corresponding Euler matrix for the director axis system

$$\mathbf{R}_{IL} = \mathbf{R}_{IB}\cdot\mathbf{R}_{BL} \qquad \text{(A2.5)}$$

Note that when the director is not parallel to the field, $P(\Omega)$ is not axially symmetric with respect to the field and the integration in eq A2.2 must be taken over all three Euler angles.

References and Notes

(1) Stehlik, D.; Mobius, K. *Annu. Rev. Phys. Chem.* **1997**, *48*, 745−784.
(2) Levanon, H.; Möbius, K. *Annu. Rev. Biophys. Biomol. Struct.* **1997**, *26*, 495−540.
(3) Turro, N. J.; Khudyakov, I. V. *Res. Chem. Intermed.* **1999**, *25*, 505−529.
(4) van der Est, A. *Biochim. Biophys. Acta* **2001,** *1507*, 212−225.
(5) Mazzoni, M.; Conti, F.; Corvaja, C. *Appl. Magn. Res.* **2000**, *18*, 351−361.
(6) Mizuochi, N.; Ohba, Y.; Yamauchi, S. *J. Phys. Chem. A* **1999**, *103*, 7749−7752.
(7) Mizuochi, N.; Ohba, Y.; Yamauchi, S. *J. Chem. Phys.* **1999**, *111*, 3479−3487.
(8) Jockusch, S.; Dedola, G.; Lem, G.; Turro, N. J. *J. Phys. Chem. B* **1999**, *103*, 9126−9129.
(9) Ishii, K.; Fujisawa, J.; Ohba, Y.; Yamauchi, S. *J. Am. Chem. Soc.* **1996**, *118*, 13079−13080.
(10) Fujisawa, J.; Ishii, K.; Ohba, Y.; Yamauchi, S.; Fuhs, M.; Mobius, K. *J. Phys. Chem. A* **1999**, *103*, 213-216.
(11) Fujisawa, J.; Ishii, K.; Ohba, Y.; Yamauchi, S.; Fuhs, M.; Mobius, K. *J. Phys. Chem. A* **1999**, *103*, 3138.
(12) Hore, P. J.; Riley, D. J.; Semlyen, J. J.; Zwanenburg, G.; Hoff, A. J. *Chem. Phys. Lett.* **1993**, *1141*, 221−230.
(13) Till, U.; Klenina, I. B.; Proskuryakov, II.; Hoff, A. J.; Hore, P. J. *J. Phys. Chem. B* **1997**, *101*, 10939−10948.
(14) Salikhov, K. M.; van der Est, A. J.; Stehlik, D. *Appl. Magn. Res.* **1999**, *16*, 101−134.
(15) Blank, A.; Levanon, H. *J. Phys. Chem. A* **2000**, *104*, 794−800.
(16) Corvaja, C.; Sartori, E.; Toffoletti, A.; Formaggio, F.; Crisma, M.; Toniolo, C.; Mazaleyrat, J. P.; Wakselman, M. *Chem. Euro. J.* **2000**, *6*, 2775−2782.
(17) Blank, A.; Levanon, H. *J. Phys. Chem. A* **2001**, *105*, 4799−4807.
(18) Fujisawa, J.; Ishii, K.; Ohba, Y.; Yamauchi, S.; Fuhs, M.; Mobius, K. *J. Phys. Chem. A* **1997**, *101*, 5869−5876.
(19) Conti, F.; Corvaja, C.; Toffoletti, A.; Mizuochi, N.; Ohba, Y.; Yamauchi, S.; Maggini, M. *J. Phys. Chem. A* **2000**, *104*, 4962−4967.
(20) Asano-Someda, M.; van der Est, A.; Krüger, U.; Stehlik, D.; Kaizu, Y.; Levanon, H. *J. Phys. Chem. A* **1999**, *103*, 6704−6714.
(21) Asano-Someda, M.; Ichino, T.; Kaizu, Y. *J. Phys. Chem. A* **1997**, *101*, 4484−4490.
(22) Ohno, O.; Ogasawara, Y.; Asano, M.; Kajii, Y.; Kaizu, Y.; Obi, K.; Kobayashi, H. *J. Phys. Chem.* **1987**, *91*, 4269.
(23) Stehlik, D.; Bock, C. H.; Thurnauer, M. C. Transient EPR−Spectroscopy of Photoinduced Electronic Spin States in Rigid Matrixes. In

Advanced EPR in Biology and Biochemistry; Hoff, A. J., Ed.; Elsevier: Amsterdam, 1989; pp 371−403.

(24) van der Est, A.; Hager-Braun, C.; Leibl, W.; Hauska, G.; Stehlik, D. *Biochim. Biophys. Acta* **1998**, *1409*, 87−98.

(25) Gonen, O.; Levanon, H. *J. Phys. Chem.* **1985**, *89*, 1637.

(26) Gonen, O.; Levanon, H. *J. Chem. Phys.* **1986**, *84*, 4132−4141.

(27) van der Est, A. J.; G. Fuechsle; D. Stehlik; Wasielewski, M. R. *Appl. Magn. Res.* **1997**, *13*, 317−335.

(28) Closs, G. L.; Forbes, M. D. E.; Norris, J. R. *J. Phys. Chem.* **1987**, *91*, 3592−3599.

(29) Fujisawa, J.; Ohba, Y.; Yamauchi, S. *J. Phys. Chem. A* **1997**, *101*, 434−439.

(30) Note: the fitting for the *Z*′-orientation was carried out so that the ratio of the absolute intensity for the ISC contribution in the $\lambda_{ex} = 540$ nm trace versus the amplitude of the $\lambda_{ex} = 640$ nm signal trace is the same as that at the *X*′ position. This is because the 540 nm excitation gives the same amount of the direct excitation of the free base at all the magnetic fields, and the signal time trace of the direct ISC pathway should not change at each field position with a change of the excitation wavelength.

(31) Jeoung, S. C.; Takeuchi, S.; Tahara, T.; Kim, D. *Chem. Phys. Lett.* **1999**, *309*, 369−376.

(32) Kobayashi, T.; Huppert, D.; Straub, K. D.; Rentzepis, P. M. *J. Chem. Phys.* **1979**, *70*, 1720−1726.

(33) Rodriguez, J.; Kirmaier, C.; Holten, D. *J. Am. Chem. Soc.* **1989**, *111*, 6500−6506.

(34) de Lange, C. A.; Snijders, J. G.; Burnell, E. E. On the Orientation of Small Molecules in Anisotropic Solvents. In *Nuclear Magnetic Resonance of Liquid Crystals*; Emsley, J. W., Ed.; D. Reidel: Dordrecht, 1985; pp 181−205.